Finite Element-Based Damage Tolerance Methods for Aircraft Composites

Yuri Nikishkov, Andrew Makeev*
School of Aerospace Engineering, Georgia Institute of Technology, Atlanta, GA

Christopher Cline, John Beasley, and Russ Fay
Boeing, Philadelphia, PA

ABSTRACT

Solid finite element-based techniques have been successfully used for simulation of the matrix-dominated failure modes in composites. Such techniques do not require initial flaws for the damage prediction. The main objective of this work is to show the ability of solid finite element-based techniques to accurately predict the onset and progression of damage under quasi-static and fatigue loading. The specific objectives are: (a) to develop failure simulation models of multidirectional carbon/epoxy laminate articles in a finite element code; and (b) to correlate the failure predictions with test data. The test articles include a 16-ply IM7/8552 tape open-hole tensile coupon, a hybrid Ti, carbon/epoxy and glass/epoxy coupon, and a hybrid carbon/epoxy and glass/epoxy lug coupon. Available stress-strain relations and failure criteria are built in ABAQUS models, and fatigue curves are used to predict the number of cycles to fatigue damage onset and progression. Model predictions and subsequent test correlations are presented.

INTRODUCTION

Currently, durability and damage tolerance of composite structures is demonstrated through component testing. No analytical damage tolerance substantiation methodologies have been used to certify composite parts. Industry, government labs, and academia have conducted significant research efforts to utilize fracture mechanics principles to characterize and predict delamination failures in composites. Interlaminar fracture mechanics methods have been developed to predict delamination growth onset from a simulated initial delamination. Acceptance of such techniques requires successful demonstration at the structural level. One concern is that defining component failure as the onset of delamination growth from initial delamination flaw might prove overly conservative. This is true because energy absorbing mechanisms, other than delamination, may occur in structural components for a variety of reasons, such as branching of the initial delamination through matrix ply cracks into other interfaces in tape laminates. Accurate damage tolerance models must account for in-ply as well as interlaminar failure modes and their interaction.

This work summarizes collaborative efforts at Georgia Tech and Boeing to develop and verify damage tolerance methods for composites. Three-dimensional solid finite element-based techniques attractive for simulation of the matrix-dominated failure modes are presented. Stress-based and fracture mechanics-based failure criteria are used to predict the matrix-dominated failures. Material stiffness loss consistent with the failure criteria is implemented in the 3D solid FE-based failure models for simulation of the matrix-ply cracks. Initial damage and a predefined path are not required.

Multiple practical examples are presented. First, damage initiation and growth simulations under static and fatigue loading conditions for open-hole tensile quasi-isotropic IM7/8552 Carbon/Epoxy laminate articles are accomplished. Damage sequence, surface strains and failure loads are verified with tests utilizing the digital image correlation technique. Second, the analysis of hybrid Glass and Carbon/Epoxy laminate with Titanium is provided. Finally, the damage simulation is provided for the loaded hole geometry in the hybrid Glass and Carbon/Epoxy laminate. Damage sequence and failure load predictions are verified with tests.

The computational models developed in this work are implemented through custom material and element procedures in the ABAQUS finite element code. Extensive scripting capability provided by ABAQUS/CAE pre-processing software allows for parametric generation of the complex geometries, finite element meshes and element properties.

DAMAGE ANALYSIS

This section presents the foundations of the damage simulation method presented in this paper. The method is based on the following principles:

- Microscopic damage: accounted for by accurate material non-linearity measurements.
- Matrix failure criterion: stress-based failure criterion relates stresses to material strength.
- Delamination analysis: stress-based failure criterion for 3D stress state used in the thin layer of elements between the laminate plies.
- Failure simulation: element failure is simulated by decreasing stiffness in the directions defined by failure criterion.

* Corresponding Author. Address, School of Aerospace Engineering, Georgia Tech, 270 Ferst Dr., Atlanta, GA 30332-0150; Phone, 14048948166; Email, andrew.makeev@aerospace.gatech.edu
Presented at the 36th European Rotorcraft Forum, Paris, France, September 7-9, 2010.

- Progressive fatigue damage algorithm: based on the linear damage accumulation, the algorithm combines strength adjustment based on S-N curves and accumulated damage to find true fatigue failure.

Microscopic Damage

Tests show that composite materials demonstrate highly nonlinear shear stress-strain response before detectable matrix-ply cracking. Physically, shear nonlinearity can correspond to micro-cracks in the matrix. Makeev [1] used full-field strain measurement to generate accurate shear stress-strain response approximation for IM7/8552 Carbon/Epoxy tape in the form of Ramberg-Osgood equation:

$$\gamma_{12} = \tau_{12} / G_{12} + (\tau_{12} / K_{12})^{1/n} \quad (1)$$

An n = 0.2 value generated in [1] results in the 5th-order nonlinearity in the shear stress-strain response.

Matrix Failure Criterion for Macroscopic Damage

Stress-based failure criteria are used to establish failure initiation. This work uses the Fracture toughness-based criterion [2] adjusted to account for the nonlinear stress-strain response [3]:

$$\begin{aligned} &(1-g)\frac{\sigma_{22}}{S_{22}} + g\left(\frac{\sigma_{22}}{S_{22}}\right)^2 + \frac{\chi(\tau_{12})}{\chi(S_{12})} = 1, \quad \sigma_{22} > 0 \\ &\frac{\chi(\tau_{12})}{\chi(S_{12})} = 1, \quad \sigma_{22} \le 0 \end{aligned} \quad (2)$$

where $g = G_{Ic} / G_{IIc}$, and G_{Ic}, G_{IIc} are Mode I and Mode II fracture toughness values and $\chi(\tau_{12})$ is a shear component of the strain energy density

$$\chi(\tau_{12}) = 2\int \tau_{12} d\gamma_{12}(\tau_{12})$$

For the non-linear shear response (Eq. 1) this function is integrated:

$$\chi(\tau_{12}) = \frac{\tau_{12}^2}{G_{12}} + \frac{2K}{n+1}\left(\frac{\tau_{12}}{K}\right)^{\frac{1}{n}+1} \quad (3)$$

In the example below, the Fracture toughness-based criterion performance is compared to the Hashin failure criterion [4].

Delamination Analysis

Simulating delamination failures is important for accurate damage predictions even if the specimen failures are dominated by matrix cracking. Significant interactions between matrix and interlaminar damage modes are confirmed by tests and numerical results presented in this work.

Delamination failures are simulated by applying the stress-based failure criterion to the elements located in the thin layer between the laminate plies. The cracks are assumed to propagate in 1-3 material plane; therefore the same matrix failure criterion can be used provided that material directions 2 and 3 are interchanged. The delamination layer is in three-dimensional stress state and all three stress components must be accounted for in the criterion. For delamination failures the Fracture toughness-based criterion (Eq. 2) takes the following form:

$$\begin{aligned} &(1-g)\frac{\sigma_{33}}{S_{33}} + g\left(\frac{\sigma_{33}}{S_{33}}\right)^2 + \frac{\chi(\tau_{13})}{\chi(S_{13})} + \frac{\chi(\tau_{23})}{\chi(S_{23})} = 1, \quad \sigma_{33} > 0 \\ &\frac{\chi(\tau_{13})}{\chi(S_{13})} + \frac{\chi(\tau_{23})}{\chi(S_{23})} = 1, \quad \sigma_{22} \le 0 \end{aligned} \quad (4)$$

Transverse interlaminar shear strength S_{23} is calculated from the transverse compressive strength using the approach from [2]:

$$S_{23} = S_{22C} / 2\tan\alpha_0 \quad (5)$$

where α_0=53° is the typical fracture plane angle for compressive failures.

Failure Simulation

Stress-based failure criteria are used to establish initiation of a crack "smeared" over a single finite element. After a failure criterion is met the element is assumed broken for the rest of the analysis. Failed state of a solid element for matrix-ply crack simulation assumes loss of element stiffness in the plane of cracking as defined by the initiation criterion. Following this assumption, the element loses tensile stiffness in the transverse material direction (2) as well as shear stiffness in the (1-2) and (2-3) planes. Following the approach by Kachanov [5] the stiffness modulus decreases with damage:

$$E_d = E/(1 - d) \quad (6)$$

where d represents the damage variable. For more details on the stress-strain relationship in the damaged elements, see [6].

It is assumed that under tension the damage variable d goes from zero to one as fast as practically possible to allow for convergence of the numerical procedure. The damage variable is expressed as

$$d(t) = \begin{cases} 0, t < t_f \\ (1-k_f)\dfrac{t-t_f}{\Delta t_r}, t_f \le t \le t_f + \Delta t_r \\ 1 - k_f, t > t_f + \Delta t_r \end{cases} \quad (7)$$

where t represents time parameter in the quasi-static FE analysis. t_f corresponds to the time parameter for which the element failed; Δt_r is the time of damage relaxation determined from convergence requirements; and k_f is the remaining stiffness ratio that is small enough to simulate the complete element failure. The time variable can be proportional to the load for the static analysis or to the increment number in the fatigue analysis. In the fatigue damage progression algorithm proposed below, time parameter is proportional to the number of elements failed in the increment. Convergence of the equilibrium iterations also requires that the non-linear adjustment of the shear moduli continues until the element is fully damaged.

Fatigue Damage Progression Algorithm

As proposed by Hashin [7] the in-plane shear and tensile strength values in the fatigue failure criteria are assumed to follow the material S-N curves for interlaminar shear and tensile values (see Material Properties section)

$$S_{22} = S_{22,static}\,0.9001(\log N)^{-0.3504}$$
$$S_{12} = S_{12,static}\,1.2487(\log N)^{-0.4123} \quad (8)$$

where $S_{22,static}$ and $S_{12,static}$ are static in-plane tensile and shear strengths.

To calculate the number of cycles to failure in a finite element-based model, Equations (8) are substituted in the failure criterion (2) to calculate cycles to failure for each element. The minimum number of cycles corresponds to initiation of macroscopic damage.

Fatigue damage progression algorithm is based on the combination of the fatigue failure criterion predictions with the damage accumulation due to fatigue cycling. At any cycle, the fatigue failure criterion is assumed to provide the "undamaged" cycle to failure, while the true "damaged" solution is obtained from the assumption of critical damage value accumulated linearly over the cycles.

Fatigue damage progression algorithm proceeds as follows:

1. Apply maximum fatigue load to the model. Obtain stresses at zero cycles.

2. For each element solve the algebraic equation for the number of cycles obtained by substituting fatigue curves (Eq. 5) for the strength values in the failure initiation criterion.

$$F\left(\sigma_{el}^{(k)}, S\left(N_{el}^{f}\right)\right) = 1 \quad (9)$$

where $F(\sigma, S)$ denotes stress-based failure criterion, $\sigma^{(k)}$ is current stress state in the element and $S(N^f)$ are strengths adjusted using fatigue curves (Eq. 7). Solution N^f is the number of cycles to failure for the undamaged material in the current stress state. For the failure criterion used in this work (Eq. 2) this equation has monotone derivative, so that it always has single root.

3. For each element find progressive failure cycle N^{pf} based on the linear accumulation of damage from the previous steps, and assuming that failure occurs when damage reaches critical value:

$$N_{el}^{pf} = (d^{f} - d_{el}^{(k-1)})N_{el}^{f} \quad (10)$$

In this work d^f is assumed equal to unity.

4. Find minimum N^{pf} (denote it as $N^{(k)}$) for the first element failure.

5. Advance cycle counter by $N^{(k)}$ and for each non-failed element calculate current fatigue damage (using linear damage accumulation principle):

$$d_{el}^{(k)} = d_{el}^{(k-1)} + \frac{N^{(k)}}{N_{el}^{f}} \quad (11)$$

d=0 at zero cycles.

6. Fail the element and recalculate stresses $\sigma^{(k+1)}$.

7. Continue from step 2 until maximum cycles reached or ultimate failure criterion is satisfied.

To speed up the calculations, it is possible to fail multiple elements in a single iteration. In this case, at step 4 the elements are sorted by cycles to failure, the desired number of elements with the smallest cycles are failed, and cycle counter is advanced by the largest cycle in the group.

Computational Procedure

Numerical methods that simulate damage by reducing material stiffness are known to produce mesh-dependent results [8]. The dependence of the crack development on the mesh orientation can be especially strong in case of a structured circumferentially-oriented mesh. For example, the circumferentially-oriented mesh with the smallest element in-plane size of 0.12 mm (4.7 mil) and total 707529 DOF not only was not able to determine accurate failure loads but also was not able to capture the damage progression.

To overcome crack dependence on mesh orientation the fiber-aligned mesh approach was used [6]. Finite element mesh for each ply is structured such that the mesh line directions are parallel to the fiber directions. Since ply meshes are incompatible at their interfaces, mesh tie constraints are used to hold the mesh assembly together. Mesh tie constraints introduce additional equations that relate slave degrees of freedom for a ply to the corresponding degrees of freedom at the projected point for a neighbor ply.

MATERIAL PROPERTIES

This section presents the material stress-strain response and fatigue properties based on the tests of unidirectional specimens.

Table 1 lists stiffness and strength properties according to [1], and fracture toughness values per [9]. Note that secant-intercept modulus and exponent refer to an approximation of the shear stress-strain response given in Eq. 1.

Table 1. Material properties for IM7/8552 Carbon/Epoxy tape.

Tensile modulus, E_{11}	171 GPa (24.8 msi)
Tensile modulus, $E_{22}=E_{33}$	8.96 GPa (1.3 msi)
Poisson's ratio, $\nu_{12}=\nu_{13}$	0.32
Poisson's ratio, ν_{23}	0.5
Shear modulus, $G_{12}=G_{13}$	5.31 GPa (0.77 msi)
Shear modulus, $G_{23}= E_{22}/(2*(1+\nu_{23}))$	2.99 GPa (0.433 msi)
Secant-intercept modulus, $K_{12}=K_{13}$	260 MPa (37.8 ksi)
Secant-intercept modulus, $K_{23} = K_{12}*G_{23}/G_{12}$	147 MPa (21.3 ksi)
Exponent, n	0.203
Transverse tensile strength, Y^T	98.6 MPa (14.3 ksi)
Shear strength, S^L	113 MPa (16.4 ksi)
Mode I fracture toughness, G_{Ic}	0.2774 kJ/m^2 (1.584 psi*in)
Mode II fracture toughness, G_{IIc}	0.7889 kJ/m^2 (4.505 psi*in)

Figure 1 shows a SBS test setup and a shear strain measurement.

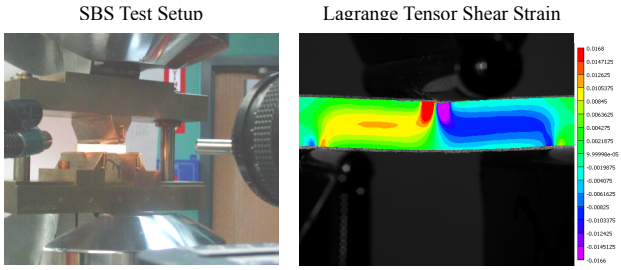

Figure 1. SBS Test Setup and Full-Field Strain Measurement.

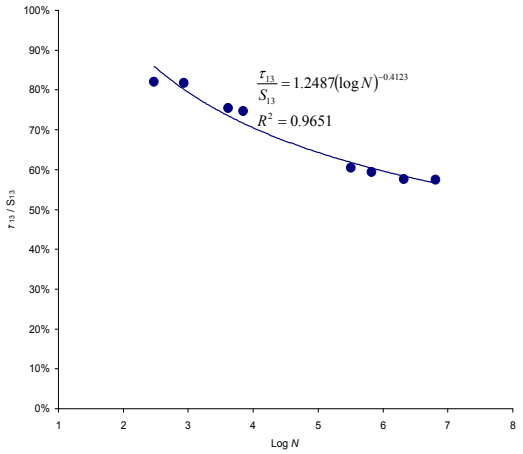

Figure 2. Interlaminar (1-3 Plane) Shear S-N Curve for Unidirectional IM7/8552 Tape

To generate the interlaminar shear fatigue curve, constant load amplitude SBS fatigue tests at 0.1 load ratio and 10 Hz frequency were conducted. A shear fatigue delamination failure close to the mid-surface of the coupons could not be obtained using the static SBS test coupon dimensions. Matrix compressive damage under the loading nose of the test fixture resulted in delamination close to the coupon upper surface. To reduce the compressive loads, the dimensions of the fatigue SBS test coupons used in this work were modified to 0.15 inch thickness (3.8 mm), 0.12 inch width (3.0 mm), and 0.76 inch length (19.3 mm). The loading nose roller diameter in the ASTM Standard D 2344 SBS test fixture was also modified from 0.25 inches (6.35 mm) to 0.5 inches (12.7 mm). A shear delamination was established for all fatigue SBS tests except one that took close to 10 million cycles to delamination onset.

Figure 2 shows the interlaminar shear stress at peak loads as a function of cycles to delamination onset. A power law

$$\frac{\tau_{13}}{S_{13}} = 1.2487(\log N)^{-0.4123} \qquad (12)$$

approximates the average response based on a linear regression. Five static SBS tests were also conducted to confirm the constitutive properties for the modified SBS test configuration. Table 2 lists the static strength and stiffness parameters.

Table 2. Interlaminar (1-3 Plane) Shear Strength and Stiffness Values for the Modified SBS Test Configuration.

	AVG	COV
S_{13}, MPa (ksi)	110 (16)	2%
G_{13}, MPa (ksi)	5.32 (0.771)	4%
K, MPa (ksi)	247 (35.8)	4.86%
n	0.208	4.95%

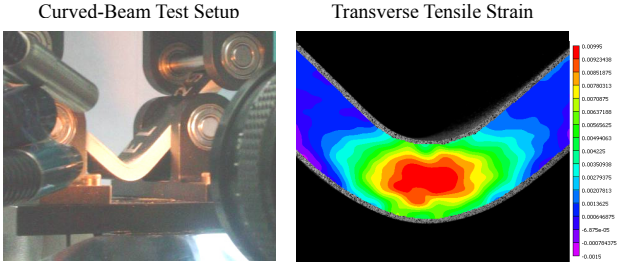

Figure 3. Curved-Beam Test Set-up and Full-Field Strain Measurement

The interlaminar tensile constitutive properties were generated based on curved-beam tests. Five static and six fatigue unidirectional IM7/8552 tape curved-beam coupons were tested. The coupons were manufactured to ASTM Standard specifications [10], except the width was reduced from 1 inch (25.4 mm) to 0.5 inches (12.7 mm). The curved-beam coupons are 0.26-inches-thick (6.6 mm). Figure 3 shows a curved-beam test setup and a transverse tensile strain measurement.

The DIC technique was used for assessment of surface strain. A closed-form solution [10] was used for interlaminar stress approximation.

The failure mode for the curved-beam test coupons was a tensile delamination. The interlaminar tensile stress-strain response was linear till failure. The average value for the interlaminar tensile modulus E_{33} is 1.3 msi (8.96 GPa) and the coefficient of variation is 3.55%. The average value for the curved-beam interlaminar tensile strength S_{33} is 12 ksi (82.7 MPa) and the coefficient of variation is 7.78%.

To generate the interlaminar tensile fatigue curve, constant load amplitude curved-beam tests at 0.1 load ratio and 5 Hz frequency were conducted. Figure 4 shows the interlaminar tensile stress at peak loads as a function of cycles to delamination onset.

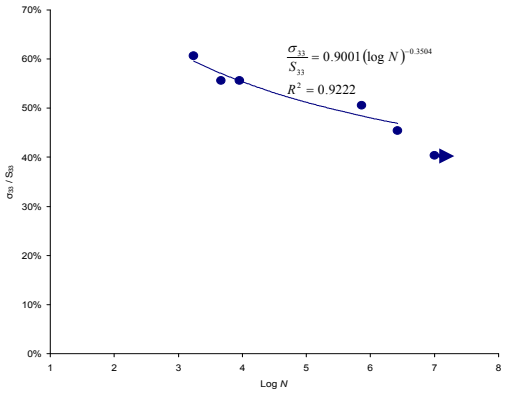

Figure 4. Interlaminar (1-3 Plane) Tensile S-N Curve for Unidirectional IM7/8552 Tape.

A power law

$$\frac{\sigma_{33}}{S_{33}} = 0.9001(\log N)^{-0.3504} \qquad (13)$$

approximates the average fatigue behavior. Equations (12) and (13) are used to predict fatigue failure onset based on failure criteria listed in the previous section.

FINITE ELEMENT SIMULATIONS

This section presents the comparison of finite element simulation results with tests for the following problems:

- Static loading of Open Hole Tensile coupons;
- Fatigue of Open Hole Tensile coupons;
- Static loading of hybrid Ti, carbon/epoxy and glass epoxy coupons;
- Static loading of hybrid carbon/epoxy and glass epoxy lug coupons.

Static Loading of Open Hole Tensile Coupons

A three-dimensional solid finite element-based failure model was built for a 16-ply $[45/0/-45/90]_{2S}$ IM7/8552 Carbon/Epoxy tape open-hole tensile (OHT) coupons, manufactured and tested to the ASTM Standard D 5766 specifications. The coupon dimensions are 38.1 × 190.5 × 2.642 mm (1.5 × 7.5 × 0.104 in). The hole diameter is 6.35 mm (0.25 in). Damage patterns and surface strains obtained using Digital Image Correlation (DIC) technique [1, 6], are compared with numerical simulations.

Figure 5 shows surface-ply cracks at failure loads.

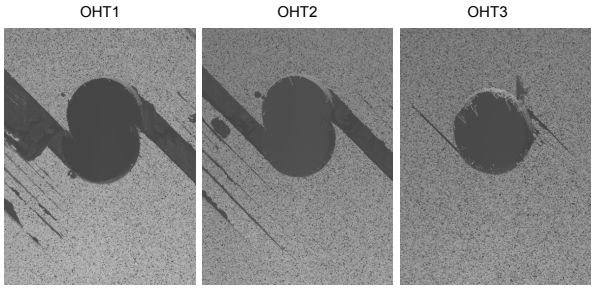

Figure 5. Surface-Ply Cracks in the OHT Coupons at Failure.

A half of the coupon through the thickness (8 plies) is considered in the analysis to reduce the computational effort. Symmetry boundary conditions were applied. Figure 6 shows a three-dimensional finite element mesh. Boundary conditions also include fixed displacements at the bottom end, and fixed transverse displacements and uniform axial (vertical) displacements with applied tensile force at the top end.

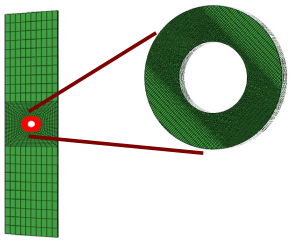

Figure 6. Global finite element mesh and the sub-model region.

The finite element model uses 8-noded three-dimensional linear elements with reduced integration (C3D8R elements in ABAQUS). Each element has a single integration point so that the damage is activated for the whole element. Reduced integration elements have been shown to adequately represent the stress state with respect to modeling damage [6]. Simulations for the OHT coupon are conducted using commercial finite element software ABAQUS, version 6.8 [11]. A custom material behavior was coded in the user-supplied subroutine UMAT. Appropriate number of elements per ply was determined by a stress convergence study [6].

Sub-modeling was used to simplify mesh generation and to allow sufficient mesh size for convergence of transverse stresses. The global mesh uses a circumferential element concentration near the hole in the coupon. The smallest finite element size in the global mesh is 0.25 mm (0.01 in) resulting in 33243 DOF. The sub-model is an assembly of fiber-aligned regular meshes. The sub-model used for comparison with tests had the outer radius equal to three times the hole radius, the smallest element size of 0.124 mm (4.9×10^{-3} in) and 4 elements per ply resulting in 92288 elements and 363120 DOF. The maximum value of load increment was selected as defined by Equation (7) with the relaxation increment Δt_r=0.4 and remaining stiffness ratio is selected as $k_f=10^{-6}$. 50 elements were allowed to fail in the single time increment of size 1.0. This failure parameter selection allows elements to fail completely in the duration of a single increment; step increment may be automatically reduced by the software to fail elements more gradually to improve convergence.

The simulation shows that the majority of the cracks are located in the 90-degree plies while the adjacent (subsurface) 45-degree plies also have more cracks than a surface 45-degree ply. However, a crack in the surface 45-degree ply ultimately grows much further than any of the other 45-degree matrix-ply cracks. Figure 7 displays the matrix-ply cracks in all layers through the thickness of the laminate based on the X-ray inspections and FEM simulation at 35.59 kN (8000 lbs).

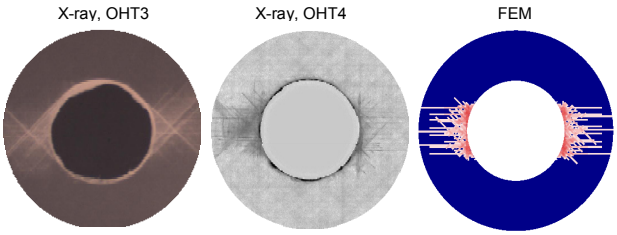

Figure 7. X-ray images and simulation results for matrix-ply cracks.

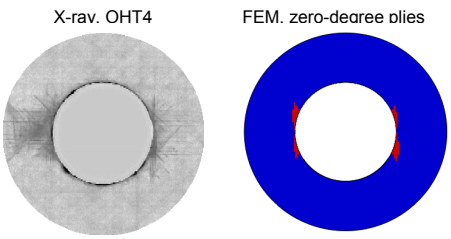

Figure 8. X-ray image and simulation results for matrix-ply cracks in the zero-degree plies at 36.92 kN (8300 lbs) tension.

Figure 8 confirms the initiation of zero-degree ply cracks at the location of the ultimate surface cracks. Figures 9 and 10 compare FEM simulation results and the test data (DIC) for surface strains in the OHT3 coupon. The Figures show the onset of cracking in the surface ply and the development of the ultimate cracks in the surface ply. Both Figures clearly show the cracks developing along the fiber direction, which is achieved in the finite element simulations through the fiber-aligned mesh.

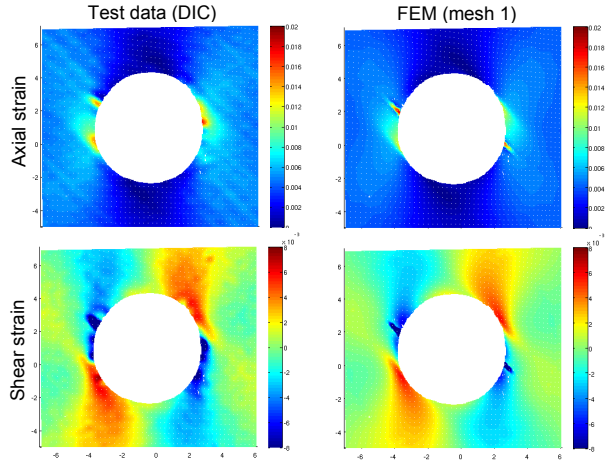

Figure 9. Surface Strains at 22.41 kN (5037 lbs) tensile load.

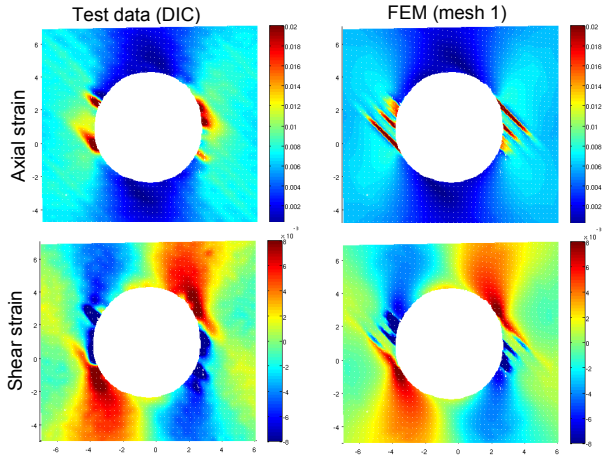

Figure 10. Surface Strains at 32.20 kN (7239 lbs) tensile load.

Table 3 lists the simulation results and test data for loads at various damage events. Figure 11 shows test data and FEM results for the surface cracks in the OHT3 coupon at the ultimate failure. The simulations show the development of the ultimate matrix-ply crack growth in two discrete steps.

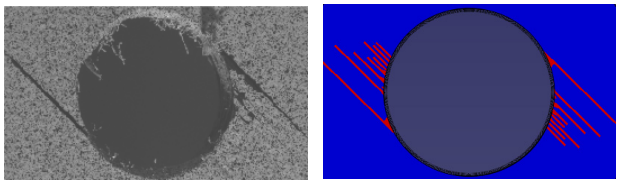

Figure 11. Test data and FEM results for surface cracks in the OHT3 coupon at ultimate failure.

Table 3. Loads at various stages of matrix-ply cracking.

Damage stage	FEM kN	Test OHT3 kN	Test AVG kN
First crack 90-degree ply	20.50		
First surface crack 45-degree ply	20.00	22.41	
Ultimate crack 45-degree ply (first discrete growth step)	28.54 (32.90)	32.53	
Ultimate failure	37.40	37.19	38.11

The fracture toughness-corrected failure criterion (Eq. 2) was used to generate the FEM results in this Section. The Hashin failure criterion [4] yields similar results for prediction of the first surface-ply crack initiation. However, the ultimate crack prediction using the Hashin criterion was not consistent. The ultimate crack is shear-dominated and Equation (3) used for the shear term assessment in the fracture toughness-corrected criterion is pertinent for ultimate failure prediction.

Fatigue of Open Hole Tensile Coupons

The coupons and FE models described in the previous section were investigated under fatigue loading conditions. The coupons were subject to constant amplitude load at 10 Hz frequency, up to 1,000,000 cycles. The minimum load was 2.22 kN (500 lbs) and the maximum load was 22.2 kN (5000 lbs).

The fatigue simulation starts with the static simulation for the maximum fatigue load. The progressive failure algorithm continues by determining the elements failed during the virtual cycles completed (as determined by the algorithm) and recalculating the stresses as a result of element damage. The elements failed during this simulation constitute the macroscopic cracks.

Figure 12 shows the comparison of the predicted matrix cracks and delaminations shown as failed elements and the CT scan of the specimen obtained after 1,000,000 cycles of fatigue loading. The Figure demonstrates excellent correlation of the locations of the major matrix cracks at the surface and sub-surface plies and delaminations between these plies. A detailed inspection of the CT scan also reveals matrix cracks in the other subsurface plies.

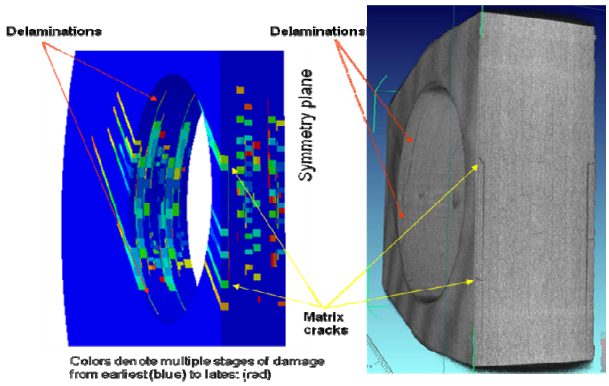

Figure 12. FE damage (right) and CT scan for the OHT coupon at 1,000,000 cycles.

Delamination is simulated by matrix failure of the thin (10% ply thickness) solid element layers between the plies. Three-dimensional Fracture toughness-based criterion accounts for interlaminar tensile and shear failure modes in both 1-3 and 2-3 material planes. Figure 13 shows the details of the damage interactions between matrix cracks and delaminations in the surface and first sub-surface plies

and their interfaces. It is worth noting that using cohesive elements for simulating delamination failures leads to significantly smaller prediction of the delamination size which contradicts the CT scan observations.

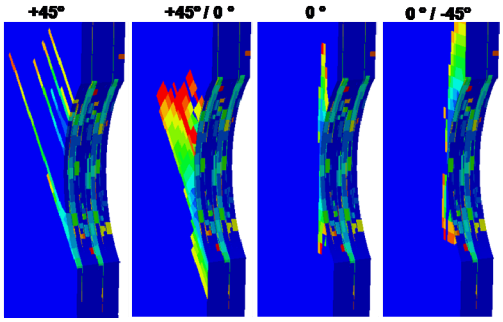

Figure 13. Slices from the surface of the specimen at 1,000,000 cycles.

The comparison of FE results with the test of the coupon obtained using DIC measurements is shown on Figure 14. The DIC image shows two major cracks on each side of the coupon as well as smaller cracks on the right side. FE damage plot displays number of elements failed early (blue to green color, N<100,000) and elements for major cracks failed at the number of cycles comparable with tests (orange to red color: 100,000<N<1,000,000). Figure 15 displays the comparison of surface strains at 1,000,000 cycles.

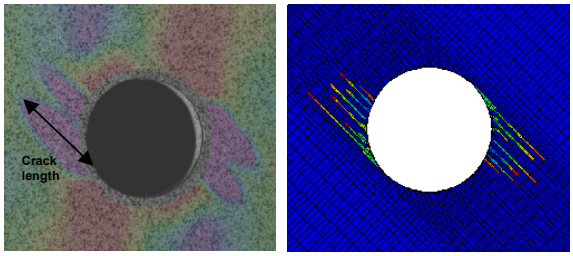

Figure 14. DIC image with overlapped shear strain (left) and FE damage (right) for the OHT coupon at 1,000,000 cycles.

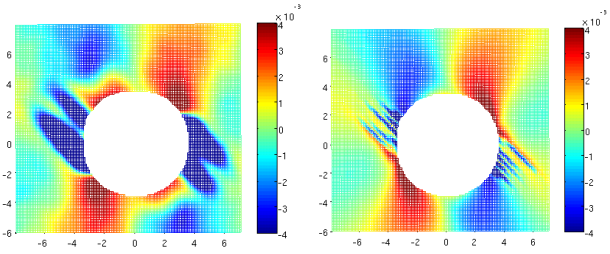

Figure 15. Shear strain from DIC (left) and FE simulation (right) at 1,000,000 cycles.

Figure 16 compares FE fatigue growth predictions of the longest surface crack based on Hashin and fracture toughness-based failure criteria with tests. Also shown are the FE crack length predictions for the model including delaminations.

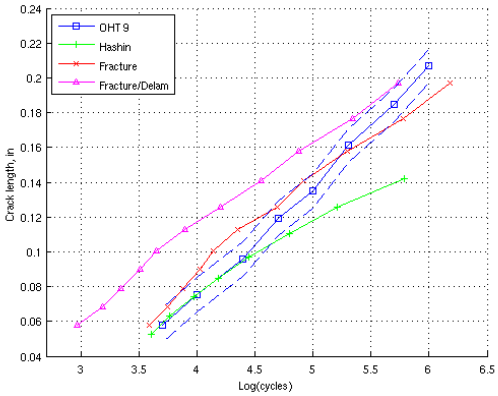

Figure 16. Comparison of the ultimate crack length versus Log (cycles) for the FE predictions and test data.

The test crack lengths were obtained by inspecting DIC images at the corresponding number of fatigue cycles and measuring length of the area of shear deformation reaching approximately 0.3%, as shown on Figure 14. As noted above, damage smearing methods are dependent on the mesh size, in particular on the size of the element that simulates growing crack. Figure 17 shows comparison of the biggest surface crack length versus Log (cycles) for different crack widths in finite element simulations. The comparison shows converging predictions with the element size decreasing. The crack obtained on the mesh with the smallest size, e = 0.105 mm, actually had smaller crack length prediction for the same cycles than the mesh with e = 0.124 mm; however, the symmetric crack on the other side of the whole had higher predictions. Both are shown on Figure 17.

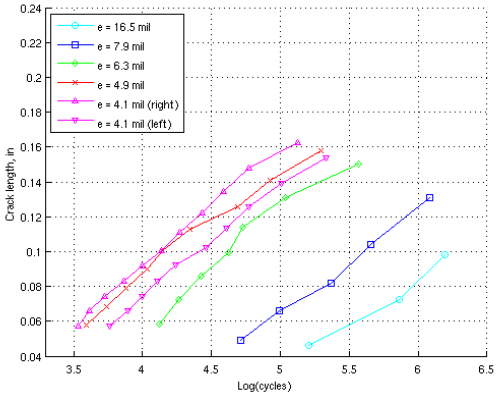

Figure 17. Comparison of the ultimate crack length versus Log (cycles) for different crack width e in FE simulations.

The figures above show very good qualitative and quantitative agreement of FE simulations with tests. The simulations are able to predict the locations of macroscopic cracks and their development for both low and high fatigue cycles. The fatigue damage progression algorithm using fracture toughness-based criterion was able to conservatively predict crack length within crack measurement tolerance for most of the fatigue test. The same algorithm using Hashin criterion has performed less conservatively and predicted significantly smaller crack lengths at high cycles. The algorithm based on fracture toughness-based criterion provides better predictions but also starts to underpredict fatigue crack length at the high cycles. Taking ply delaminations into account allows

obtaining conservative predictions when crack lengths reach larger values.

Hybrid Ti, Carbon/Epoxy and Glass/Epoxy Coupon

The hybrid Ti, carbon/epoxy and E-glass/epoxy Z-shaped specimen was tested in tension up to a 245 kN (55 kip) load. The coupon dimensions are 508 × 152 × 5.28 mm (20 × 6 × 0.208 in). Hole diameter is 12.7 mm (0.5 in). The fiber directions in the central region of the coupon are oriented at 8 degrees from the direction of the load. The hybrid layup is shown on Figure 18 (2x scale through the thickness). The Titanium layer is attached to the E-glass layer by the adhesive.

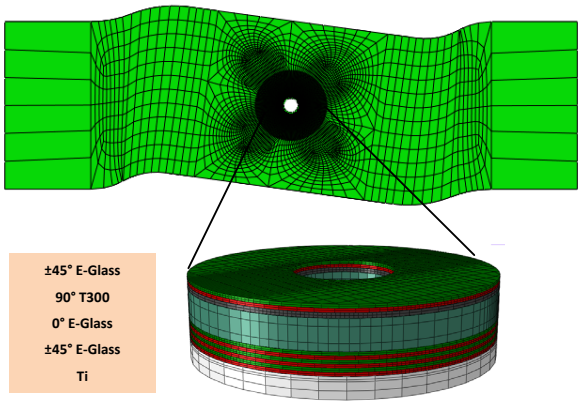

Figure 18. Global FE mesh, layup and the FE sub-model of the hybrid Z-shaped specimen.

The analysis follows the same procedure as in the previous example. Figure 18 shows the finite element mesh of the global model used for the structural analysis of the specimen and the sub-model represented by a collection of cylindrical fiber-aligned meshes around the hole. The global model allows for obtaining accurate in-plane stress distribution at the distances of the order of hole radius from the center of the hole. For efficiency, no matrix failure or delamination is simulated in the global model. The sub-model is driven by the displacements from the global mesh; matrix failures and delaminations are simulated on fiber-aligned meshes that allow crack growth in physically correct directions.

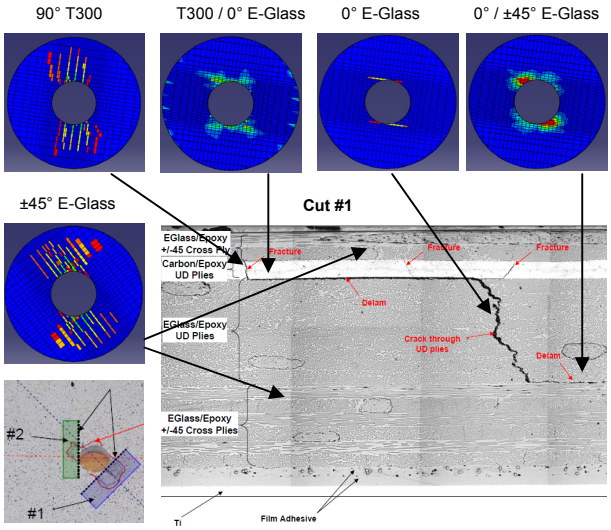

Figure 19. FE matrix damage and delaminations compared with tests at 245 kN (55 kip) static load.

Figure 19 shows comparison of the FE simulation damage results and defects in the test specimen. The Figure shows the ply and interface meshes with damaged elements shown in color (color encodes failure load). Corresponding plies and delamination interfaces are indicated on the test cut (location of the cut shown). Excellent correlation of crack and delamination locations is observed. Ultrasound-based non-destructive inspection was carried out on the test specimen to detect the size and depth of delaminations (shown as red curve on the image of the specimen surface): 5-12 mm (0.2-0.5 in) delamination around 0º E-Glass plies was observed. FE simulation predicted the delamination of size 3.8 mm (0.15 in) around 0º E-Glass plies.

Hybrid Lug Coupon

The hybrid carbon/epoxy and S-glass/epoxy lug specimen was tested in tension up to a 40 kN (9 kip) load. Coupon dimensions are 260 × 41.9 × 2.88 mm (10.25 × 1.65 × 0.1135 in). Hole diameter is 12.7 mm (0.5 in). The hybrid layup is $[[\text{Carbon } \pm 45°/\text{S-Glass } 0°]_5 \text{ S-Glass } 0°]_S$. Figure 20 shows the specimen model and the close-up of the global mesh around the hole.

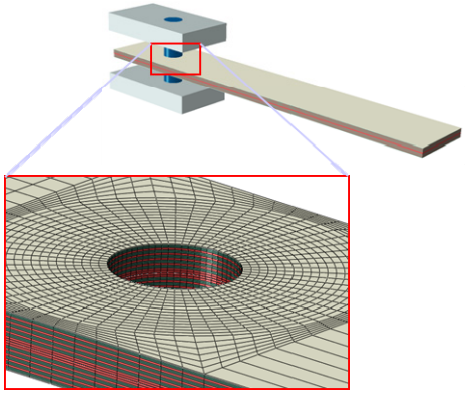

Figure 20. Global FE model of the hybrid lug specimen.

The following are the preliminary results of the application of the damage analysis to the lug coupons. The procedure described in Damage Analysis section was used for simulating matrix failures; delaminations were modeled using cohesive zone elements implemented in ABAQUS [11].

Test data shows the delamination between outer +45° and -45° plies (B) and between the 1st 0º glass ply and IM7 ±45 pack (C) as shown on Figure 21. Simulation predicts delamination occurring between outer +45° and -45° plies (A) while locations (B, C) suggest delaminations at higher loads.

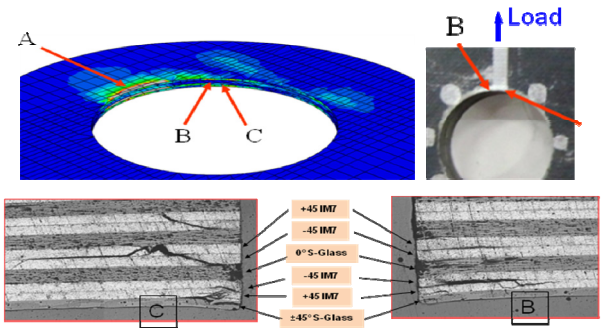

Figure 21. Comparison of the delamination predictions at 15.6 kN (3500 lbs) with tests at 33.4 kN (7500 lbs).

Test results also show matrix cracks in 0º S-Glass pack in center of layup at (C) as shown on Figure 22. Simulation predicts matrix crack initiation in 0º S-Glass pack in center of layup at 13.3 kN (3000 lbs) (A), extending radially to (B) by 15.6 kN (3500 lbs).

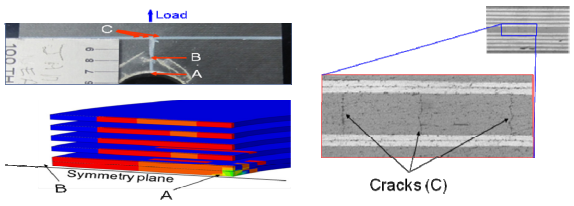

Figure 22. Comparison of matrix crack predictions at 13.3 kN (3000 lbs) with tests at 40 kN (9000 lbs).

The poor correlation of simulation and test results above is due to convergence problems in FEM equilibrium iterations arising from using cohesive zone elements. The authors plan to apply the damage analysis methodology presented in this paper to the lug coupon problem since it typically exhibits fewer convergence issues.

CONCLUSIONS

Three-dimensional solid element finite element simulation and fracture-based failure criteria have shown the ability to capture the multi-stage matrix-ply cracking and delaminations in composite laminates, including the hybrid laminates. The fatigue progression algorithm presented in this work was able to accurately capture ply cracking sequence and fatigue crack growth in the open hole tensile specimen.

The authors plan to develop comprehensive analysis tools for the simulation of composite damage and failure for the variety of applications and model geometries. Future applications of the presented methodology may include defect substantiation in thick composites and progressive failure under impact loads.

ACKNOWLEDGMENTS

This work is sponsored by the Center for Rotorcraft Innovation and the National Rotorcraft Technology Center, U.S. Army Aviation and Missile Research, Development and Engineering Center (ARMDEC) under Technology Investment Agreement W911W6-06-2-0002, entitled National Rotorcraft Technology Center Research Program. Such support is gratefully acknowledged. The views and conclusions contained in this article should not be interpreted as representing the official policies, either expressed or implied, of the AMRDEC or the U.S. Government.

REFERENCES

[1] Makeev, A., Seon, G., and Lee, E., "Failure Predictions for Carbon/Epoxy Tape Laminates with Wavy Plies," *Journal of Composite Materials*, Vol. 44, 2010, pp. 95-112.

[2] Davila, C. G., Camanho, P. P., and Rose, C. A., "Failure Criteria for FRP Laminates," Journal of Composite Materials, Vol. 39, 2005, pp. 323–345.

[3] Chang, F. K. and Chang, K. Y., "A progressive damage model for laminated composites containing stress concentration," Journal of Composite Materials, Vol. 21, 1987, pp. 834-855.

[4] Hashin, Z., "Failure Criteria for Unidirectional Fiber Composites," *Journal of Applied Mechanics*, Vol. 47, 1980, pp. 329–334.

[5] Kachanov, L. M., "Introduction to Continuum Damage Mechanics," Martinus Nijhoff Publishers, Boston, MA, 1986.

[6] Nikishkov, Y., Makeev, A., and Seon, G., "Simulation of Damage in Composites based on Solid Finite Elements," *Journal of the American Helicopter Society*, accepted for publication, 2010.

[7] Hashin, Z., "Fatigue Failure Criteria for Unidirectional Fiber Composites", *Journal of Applied Mechanics*, Vol.48, 1981, pp. 846-852.

[8] De Borst, R. "Some recent issues in computational failure mechanics," International Journal for Numerical Methods in Engineering, Vol. 52, 2001, pp. 63–95.

[9] Camanho, P. P., and Lambert, M., "Design methodology for mechanically fastened joints in laminated composite materials," *Composites Science and Technology*, Vol. 66, 2006, pp. 3004–3020.

[10] American Society for Testing and Materials, "Standard Test Method for Measuring the Curved Beam Strength of a Fiber-Reinforced Polymer-Matrix Composite," ASTM Standard D 6415/D 6415M, ASTM International, 2006.

[11] ABAQUS 6.8.1. User's Manual, ABAQUS Inc., Pawtucket, RI, USA, 2008.